LETTER

https://doi.org/10.1038/s41586-019-1152-0

A rapidly changing jet orientation in the stellar-mass black-hole system V404 Cygni

James C. A. Miller-Jones[1]*, Alexandra J. Tetarenko[2,3], Gregory R. Sivakoff[2], Matthew J. Middleton[4], Diego Altamirano[4], Gemma E. Anderson[1], Tomaso M. Belloni[5], Rob P. Fender[6], Peter G. Jonker[7,8], Elmar G. Körding[8], Hans A. Krimm[9,10], Dipankar Maitra[11], Sera Markoff[12,13], Simone Migliari[14,15], Kunal P. Mooley[6,16,17], Michael P. Rupen[18], David M. Russell[19], Thomas D. Russell[12], Craig L. Sarazin[20], Roberto Soria[1,21,22] & Valeriu Tudose[23]

Powerful relativistic jets are one of the main ways in which accreting black holes provide kinetic feedback to their surroundings. Jets launched from or redirected by the accretion flow that powers them are expected to be affected by the dynamics of the flow, which for accreting stellar-mass black holes has shown evidence for precession[1] due to frame-dragging effects that occur when the black-hole spin axis is misaligned with the orbital plane of its companion star[2]. Recently, theoretical simulations have suggested that the jets can exert an additional torque on the accretion flow[3], although the interplay between the dynamics of the accretion flow and the launching of the jets is not yet understood. Here we report a rapidly changing jet orientation—on a time scale of minutes to hours—in the black-hole X-ray binary V404 Cygni, detected with very-long-baseline interferometry during the peak of its 2015 outburst. We show that this changing jet orientation can be modelled as the Lense–Thirring precession of a vertically extended slim disk that arises from the super-Eddington accretion rate[4]. Our findings suggest that the dynamics of the precessing inner accretion disk could play a role in either directly launching or redirecting the jets within the inner few hundred gravitational radii. Similar dynamics should be expected in any strongly accreting black hole whose spin is misaligned with the inflowing gas, both affecting the observational characteristics of the jets and distributing the black-hole feedback more uniformly over the surrounding environment[5,6].

During the 2015 outburst[7] of the black-hole X-ray binary system V404 Cygni[8], we conducted high-angular-resolution radio monitoring with the Very Long Baseline Array (VLBA). Our observations (Extended Data Table 1) spatially resolved the jets in this system, on size scales of up to 5 milliarcseconds (12 a.u. at the known distance of 2.39 ± 0.14 kiloparsecs (kpc)[9]; see examples in Fig. 1). These jets evolved in both morphology and brightness on time scales of minutes.

The orientation of the jets on the plane of the sky varied between epochs, ranging between −30.6° and +5.6° east of north (Figs. 1, 2 and Extended Data Table 2). This range encompasses the orientation inferred from the position angle of the linearly polarized radio emission[10] measured during the 1989 outburst (-16 ± 6° east of north; we state all uncertainties at 1σ)[11]. Moreover, during a period of intense radio and submillimetre flaring on 22 June 2015 (ref. [12]), we observed multiple ejection events spanning a similar range of orientations over a single four-hour observation (Fig. 1), implying extremely rapid changes in the jet axis.

The time-resolved images from 22 June (see Supplementary Video) show a series of ballistically moving ejecta that persist for tens of minutes before fading below the detection threshold of approximately 10 milliJansky (mJy). The radio emission is dominated by a stationary core that is always present, allowing us to perform relative astrometry on the ejecta. The ejecta appear on both sides of the core, with proper motions ranging from 4.3 to 46.2 milliarcseconds (mas) per day (0.06–0.64c in projection, where c is the speed of light; Fig. 3), at position angles of between −28.6° and −0.23° east of north on the plane of the sky (Extended Data Figs. 1–4 and Extended Data Table 3).

Under the (standard) assumption of intrinsic symmetry, with the known distance[9] we can use the measured proper motions of corresponding pairs of approaching and receding ejecta to determine θ, the inclination angle to the line of sight, as well as the dimensionless jet speed $\beta = v/c$ (where v is velocity; see Methods). We identify three likely pairs of ejecta with consistent position angles and ejection times (denoted N2/S2, N3/S3 and N6/S6; see Fig. 3 and Extended Data Figs. 1–3), although given that their flux-density evolution cannot be fully explained by Doppler boosting of intrinsically symmetric jets (see Methods), the assumption of symmetry remains unverified. From these three pairs we determine ($\beta = 0.32 \pm 0.02$, $\theta = 40.6 \pm 2.4$°), ($\beta = 0.35 \pm 0.01$, $\theta = 32.5 \pm 1.6$°) and ($\beta = 0.48 \pm 0.01$, $\theta = 14.0 \pm 0.8$°) (Fig. 4). In all three cases the northern component is the faster moving, and must therefore be the approaching component. For unpaired ejecta, we can use the known distance to solve for $\beta \cos\theta$, subject to an assumption regarding whether the components are approaching or receding (Fig. 4). Again, we find that the jet speed or inclination angle, or both, must vary between ejection events.

The most natural interpretation for changes in jet orientation is precession, as best studied in the persistent X-ray binary SS 433. However, each individual jet component samples the orientation of the jet axis at the time of ejection only. With only 12 discrete components on 22 June, we do not have sufficient sampling to determine whether the precession is regular. Our best constraint on the precession period comes from the roughly 30° swing in position angle between ejecta pairs N2/S2 and N6/S6, which were ejected only 1.3 hours apart. This places an upper limit of 2.6 hours on the period, although the varying position angles of the intervening ejecta suggest that the true period is substantially shorter. The lower limit of order 1 second is set by the lack of any blurring motion of the point-source components over the time scale on which they are ejected (at least 0.1 second; see Methods). Regardless, given that the distribution of position angles for a precessing jet will

[1]International Centre for Radio Astronomy Research–Curtin University, Perth, Western Australia, Australia. [2]Department of Physics, University of Alberta, Edmonton, Alberta, Canada. [3]East Asian Observatory, Hilo, HI, USA. [4]School of Physics and Astronomy, University of Southampton, Southampton, UK. [5]Istituto Nazionale di Astrofisica (INAF)–Osservatorio Astronomico di Brera, Merate, Italy. [6]Astrophysics, Department of Physics, University of Oxford, Oxford, UK. [7]Netherlands Institute for Space Research (SRON), Utrecht, The Netherlands. [8]Department of Astrophysics/IMAPP, Radboud University, Nijmegen, The Netherlands. [9]Universities Space Research Association, Columbia, MD, USA. [10]National Science Foundation, Alexandria, VA, USA. [11]Department of Physics and Astronomy, Wheaton College, Norton, MA, USA. [12]Anton Pannekoek Institute for Astronomy, University of Amsterdam, Amsterdam, The Netherlands. [13]Gravitation Astroparticle Physics Amsterdam (GRAPPA) Institute, Amsterdam, The Netherlands. [14]European Space Astronomy Centre (ESAC)/European Space Agency (ESA), XMM-Newton Science Operations Centre, Madrid, Spain. [15]Institute of Cosmos Sciences of the University of Barcelona (ICCUB), Barcelona, Spain. [16]National Radio Astronomy Observatory (NRAO), Socorro, NM, USA. [17]Caltech, Pasadena, CA, USA. [18]Herzberg Astronomy and Astrophysics Research Centre, Penticton, British Columbia, Canada. [19]New York University Abu Dhabi, Abu Dhabi, United Arab Emirates. [20]Department of Astronomy, University of Virginia, Charlottesville, VA, USA. [21]School of Astronomy and Space Sciences, University of the Chinese Academy of Sciences, Beijing, China. [22]Sydney Institute for Astronomy, School of Physics, The University of Sydney, Sydney, New South Wales, Australia. [23]Institute for Space Sciences, Bucharest-Magurele, Romania. *e-mail: james.miller-jones@curtin.edu.au

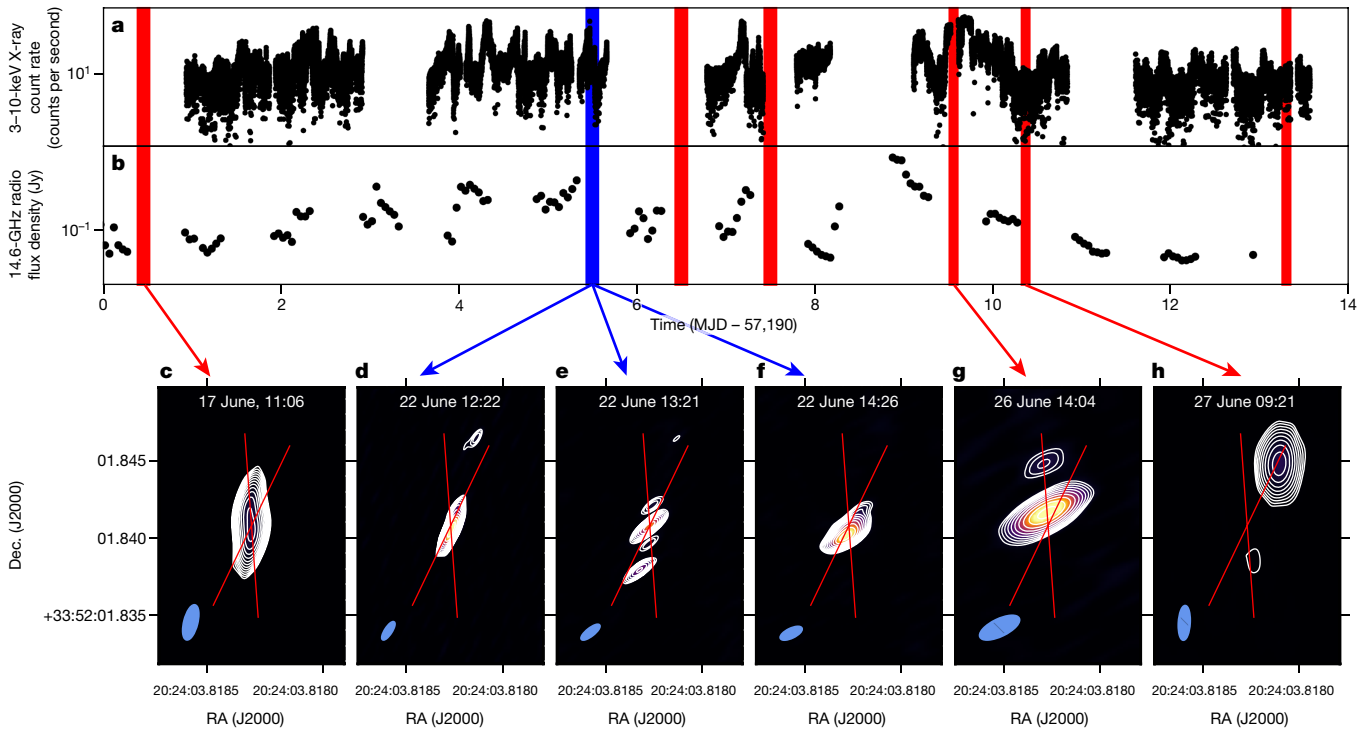

Fig. 1 | VLBA monitoring of the radio jets during the 2015 outburst of V404 Cygni. a, Count rate for 3–10-keV X-rays, from the INTEGRAL observatory[7]. **b**, 14.6-GHz radio light curve from the Arcminute Microkelvin Imager Large Array (AMI-LA) radio telescope[29]. Red and blue colours show the times of, respectively, our 8.4-GHz and 15.4-GHz VLBA observations. **c**–**h**, Snapshot VLBA images, with observing dates as indicated at the top. Blue ellipses show the synthesized beam shape, and red lines (centred on the radio core[9], which was not detected on 27 June) show the measured range of position angles (Fig. 2). The position angle of the ejecta changes over the course of the outburst, including over just a few hours on 22 June. Dec., declination; MJD − 57,190, modified Julian date minus 57,190; RA, right ascension.

peak at the two extremes, we can infer a precession-cone half-opening angle of about 18° (Fig. 2).

Because V404 Cygni probably received a kick from a natal supernova[13], a misalignment between the binary orbital plane and the black-hole spin is expected. Plasma out of the black-hole equatorial plane should then undergo Lense–Thirring precession[2], potentially affected by torques from strong magnetic fields and associated jets[3]. This phenomenon has been proposed to explain the low-frequency quasi-periodic oscillations (QPOs) observed at sub-Eddington accretion rates in many X-ray binary systems[1,14]. Regardless, both theoretical predictions and magnetohydrodynamic simulations[15] of tilted disks have shown that (at least in the absence of damping or forcing of the precession via interactions with the continuously fed outer accretion flow) a sufficiently geometrically thick disk[16] can precess as a solid body. To enable communication of the warp, the precession time scale must exceed the azimuthal sound crossing time of the disk. The viscosity and magnetic fields should also be low enough that the disk will not realign within a precession cycle[17].

During its 2015 outburst, the X-ray behaviour of V404 Cygni could be explained by invoking a geometrically thick slim-disk configuration[4]. The mass-accretion rate inferred from the peak X-ray luminosity implies a spherization (outer) radius for the slim disk consistent with the maximum for solid-body precession set by the viscous alignment time scale (see Methods). This makes Lense–Thirring precession a plausible scenario for varying the disk orientation. Precession of the inner slim disk would naturally result in precession of the jets, whether because of the magnetic field lines anchored in the precessing disk, or because of realignment of spin-powered jets, either by powerful outflows from the inner disk[18] or by the precessing slim disk itself[3].

Although the maximum radiative luminosity detected in the outburst was twice the Eddington luminosity[4], super-Eddington accretion flows are known to drive powerful winds that can carry away a large fraction of the mass flowing in from the outer disk[19], implying an outer accretion rate well above the Eddington rate. For moderate spins, mass inflow rates up to a few tens of times the Eddington accretion rate would imply precession periods[15] of up to a few minutes and spherization radii of a few tens to hundreds of gravitational radii (Extended Data Fig. 5). While such short periods would require the jet ejecta to be launched on time scales of no longer than a few seconds, they would not require the jets to exceed the Eddington luminosity over

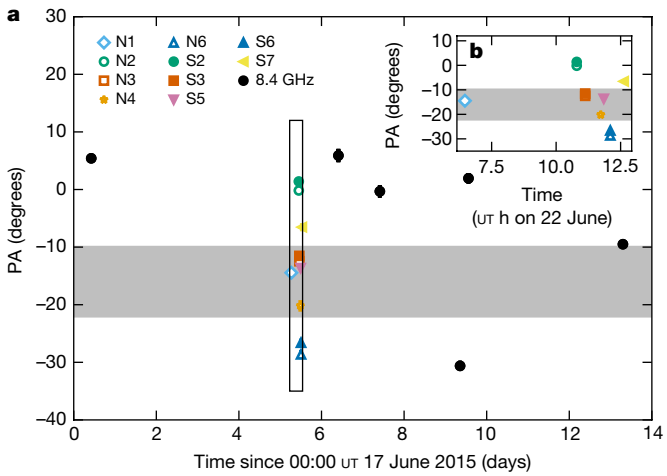

Fig. 2 | Position angles of jet components. a, Data from the full 14-day outburst period. Matched pairs of northern (N) and southern (S) components have the same colours. Uncertainties are shown at 1σ. PA, position angle. UT, universal time. **b**, Zoomed-in plot of 15.4-GHz data from 22 June 2015, corresponding to the rectangular box in panel **a**. The true precession time scale is probably substantially shorter than the 2.6-hour upper limit inferred from pairs N2/S2 and N6/S6. The grey shaded region indicates the position angle of the quiescent jet inferred from the polarized radio emission during the 1989 outburst decay[11], which is consistent with the central position angle that we measure in 2015.

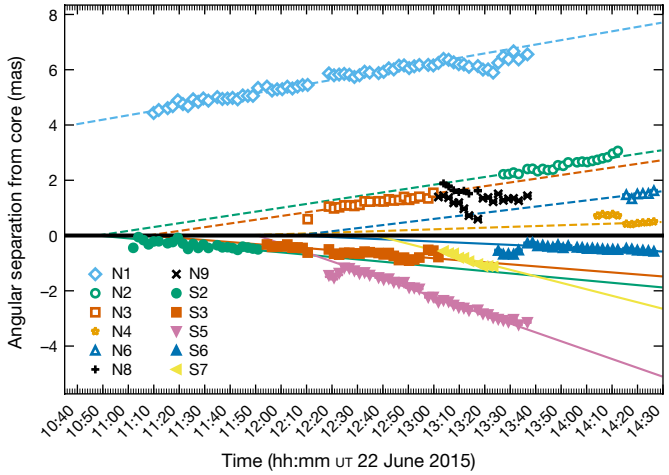

Fig. 3 | Total angular separations from the core for all jet components on 22 June 2015. Positive and negative values denote displacements to the north and south of the core, respectively. Corresponding pairs of ejecta have matching colours and marker shapes. Uncertainties (typically smaller than the marker sizes) are shown at 1σ. The best-fitting proper motions are shown as dashed lines (northern components; open markers) and solid lines (southern components; filled markers). All components except N8 and N9 move ballistically away from the core. The fitted proper motions range from 4.3 $\pm$ 0.1 mas per day to 46.2 $\pm$ 0.2 mas per day (N4 and S5, respectively). UT, universal time.

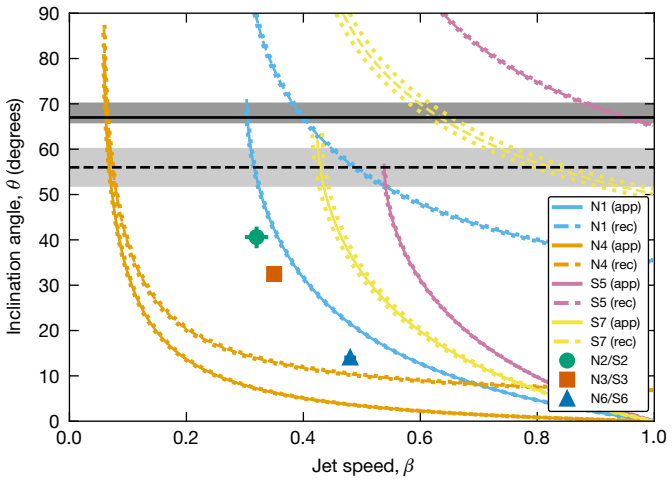

Fig. 4 | Constraints on the jet speed and inclination angle to the line of sight. Corresponding approaching (app) and receding (rec) components on 22 June 2015 allow the determination of both jet speed and inclination angle (individual points, with 1σ uncertainties). For unpaired components, the measured proper motion and source distance constrain only the product $\beta \cos\theta$, giving the plotted curves under the assumption of the components being either approaching (solid lines) or receding (dashed lines), with dotted lines showing 1σ uncertainties. The grey shading denotes the two published constraints on the orbital inclination angle[8,30], which are inconsistent with the three ejecta pairs.

the launching time scale (see Methods). The precessing jets could also give rise to optical or infrared QPOs in the optically thin synchrotron emission from the jet base.

A precessing accretion flow is also consistent with the marginal detections of short-lived low-frequency X-ray QPOs reported at 18 mHz on 22 June[20]. However, the link between the QPOs and the precessing disk is not clear and their short-lived nature would argue against long-term stable precession. In such a case, the changing mass-accretion rate (and hence spherization radius) would cause bursts of precession, subsequently damped either by disk alignment or by changes in the sound speed[3,17]. However, Fig. 2 shows that the jet axis continues to vary over our full two-week VLBA campaign. This suggests that precession continues with a relatively consistent cone-opening angle, even if the precession time scale varies.

We have observed short-timescale changes in jet orientation from a black hole accreting near the Eddington rate, probably from a reservoir whose angular momentum is misaligned with the black-hole spin. This spin-orbit misalignment in a low-mass X-ray binary suggests that the impact of black-hole natal kicks can persist even after an evolutionary phase of accretion, and could therefore affect the observed gravitational waveforms[21] during black-hole merger events arising from the evolution of isolated binary systems.

Our findings are consistent with results from recent relativistic magnetohydrodynamic simulations, which demonstrated (albeit in the absence of radiation pressure) that the accretion flow and jets precess together, owing to the combination of Lense–Thirring effects and pressure or magnetic torques from the inflow/outflow system[3]. The presence of a rapidly precessing jet in a high-accretion-rate source implies that varying jet inclination angles may need to be accounted for when interpreting observations of systems such as ultraluminous X-ray sources[22], black-hole/neutron-star mergers[23], γ-ray bursts, tidal disruption events[24], and rapidly accreting quasars in the early Universe.

Kinetic feedback from precessing jets or uncollimated winds that distribute energy over large solid angles in active galactic nuclei (AGN)[6] has been invoked to prevent the onset of cooling flows in cool core clusters[5] and to solve discrepancies between observed galactic properties and cosmological simulations[25]. For some low-luminosity AGN, which should host geometrically thick accretion flows, light-curve periodicities and helical trajectories of jet components have been suggested as direct evidence of jet precession, typically attributed to the presence of a binary supermassive black hole[26]. However, Lense–Thirring precession can also match the observed time scales (on the order of years in several cases[27,28], which, when scaled by mass, would be a good match to the time scales observed in V404 Cygni), and might be expected in chaotic accretion scenarios. Therefore, as demonstrated by our findings, precessing jets need not always signify binary black holes.

Online content

Any methods, additional references, Nature Research reporting summaries, source data, statements of data availability and associated accession codes are available at https://doi.org/10.1038/s41586-019-1152-0.

Received: 29 August 2018; Accepted: 6 February 2019;
Published online 29 April 2019.

1. Ingram, A. et al. A quasi-periodic modulation of the iron line centroid energy in the black hole binary H1743–322. *Mon. Not. R. Astron. Soc.* **461**, 1967–1980 (2016).
2. Lense, J. & Thirring, H. Über den Einfluß der Eigenrotation der Zentralkörper auf die Bewegung der Planeten und Monde nach der Einsteinschen Gravitationstheorie. *Phys. Z.* **19**, 156–163 (1918).
3. Liska, M. et al. Formation of precessing jets by tilted black hole discs in 3D general relativistic MHD simulations. *Mon. Not. R. Astron. Soc.* **474**, L81–L85 (2018).
4. Motta, S. E. et al. Swift observations of V404 Cyg during the 2015 outburst: X-ray outflows from super-Eddington accretion. *Mon. Not. R. Astron. Soc.* **471**, 1797–1818 (2017).
5. Vernaleo, J. C. & Reynolds, C. S. AGN feedback and cooling flows: problems with simple hydrodynamic models. *Astrophys. J.* **645**, 83–94 (2006).
6. Falceta-Gonçalves, D., Caproni, A., Abraham, Z., Teixeira, D. M. & de Gouveia Dal Pino, E. M. Precessing jets and X-ray bubbles from NGC 1275 (3C 84) in the Perseus galaxy cluster: a view from three-dimensional numerical simulations. *Astrophys. J.* **713**, L74–L78 (2010).
7. Rodriguez, J. et al. Correlated optical, X-ray, and γ-ray flaring activity seen with INTEGRAL during the 2015 outburst of V404 Cygni. *Astron. Astrophys.* **581**, L9 (2015).
8. Shahbaz, T. et al. The mass of the black hole in V404 Cygni. *Mon. Not. R. Astron. Soc.* **271**, L10–L14 (1994).
9. Miller-Jones, J. C. A. et al. The first accurate parallax distance to a black hole. *Astrophys. J.* **706**, L230–L234 (2009).
10. Corbel, S. et al. Coupling of the X-ray and radio emission in the black hole candidate and compact jet source GX 339-4. *Astron. Astrophys.* **359**, 251–268 (2000).
11. Han, X. & Hjellming, R. M. Radio observations of the 1989 transient event in V404 Cygni (=GS 2023+338). *Astrophys. J.* **400**, 304–314 (1992).

12. Tetarenko, A. J. et al. Extreme jet ejections from the black hole X-ray binary V404 Cygni. *Mon. Not. R. Astron. Soc.* **469**, 3141–3162 (2017).
13. Miller-Jones, J. C. A. et al. The formation of the black hole in the X-ray binary system V404 Cyg. *Mon. Not. R. Astron. Soc.* **394**, 1440–1448 (2009).
14. Stella, L. & Vietri, M. Lense–Thirring precession and quasi-periodic oscillations in low-mass X-ray binaries. *Astrophys. J.* **492**, L59–L62 (1998).
15. Fragile, P. C., Blaes, O. M., Anninos, P. & Salmonson, J. D. Global general relativistic magnetohydrodynamic simulation of a tilted black hole accretion disk. *Astrophys. J.* **668**, 417–429 (2007).
16. Papaloizou, J. C. B. & Terquem, C. On the dynamics of tilted discs around young stars. *Mon. Not. R. Astron. Soc.* **274**, 987–1001 (1995).
17. Motta, S. E., Franchini, A., Lodato, G. & Mastroserio, G. On the different flavours of Lense–Thirring precession around accreting stellar mass black holes. *Mon. Not. R. Astron. Soc.* **473**, 431–439 (2018).
18. Begelman, M. C., King, A. R. & Pringle, J. E. The nature of SS 433 and the ultraluminous X-ray sources. *Mon. Not. R. Astron. Soc.* **370**, 399–404 (2006).
19. Poutanen, J., Lipunova, G., Fabrika, S., Butkevich, A. G. & Abolmasov, P. Supercritically accreting stellar mass black holes as ultraluminous X-ray sources. *Mon. Not. R. Astron. Soc.* **377**, 1187–1194 (2007).
20. Huppenkothen, D. et al. Detection of very low-frequency, quasi-periodic oscillations in the 2015 outburst of V404 Cygni. *Astrophys. J.* **834**, 90 (2017).
21. Apostolatos, T. A., Cutler, C., Sussman, G. J. & Thorne, K. S. Spin-induced orbital precession and its modulation of the gravitational waveforms from merging binaries. *Phys. Rev. D* **49**, 6274–6297 (1994).
22. Middleton, M. J. et al. Lense–Thirring precession in ULXs as a possible means to constrain the neutron star equation of state. *Mon. Not. R. Astron. Soc.* **475**, 154–166 (2018).
23. Stone, N., Loeb, A. & Berger, E. Pulsations in short gamma ray bursts from black hole-neutron star mergers. *Phys. Rev. D* **87**, 084053 (2013).
24. Lei, W.-H., Zhang, B. & Gao, H. Frame dragging, disk warping, jet precessing, and dipped X-ray light curve of Sw J1644+57. *Astrophys. J.* **762**, 98 (2013).
25. Weinberger, R. et al. Simulating galaxy formation with black hole driven thermal and kinetic feedback. *Mon. Not. R. Astron. Soc.* **465**, 3291–3308 (2017).
26. Caproni, A. & Abraham, Z. Can long-term periodic variability and jet helicity in 3C 120 be explained by jet precession? *Mon. Not. R. Astron. Soc.* **349**, 1218–1226 (2004).
27. Nagai, H. et al. VLBI monitoring of 3C 84 (NGC 1275) in early phase of the 2005 outburst. *Publ. Astron. Soc. Jpn.* **62**, L11–L15 (2010).
28. Britzen, S. et al. OJ287: deciphering the 'Rosetta stone' of blazars. *Mon. Not. R. Astron. Soc.* **478**, 3199–3219 (2018).
29. Muñoz-Darias, T. et al. Regulation of black-hole accretion by a disk wind during a violent outburst of V404 Cygni. *Nature* **534**, 75–78 (2016).
30. Khargharia, J., Froning, C. S. & Robinson, E. L. Near-infrared spectroscopy of low-mass X-ray binaries: accretion disk contamination and compact object mass determination in V404 Cyg and Cen X-4. *Astrophys. J.* **716**, 1105–1117 (2010).

Acknowledgements The National Radio Astronomy Observatory is a facility of the National Science Foundation operated under cooperative agreement by Associated Universities, Inc. J.C.A.M.-J. is the recipient of an Australian Research Council Future Fellowship (FT140101082) funded by the Australian Government. A.J.T. is supported by a Natural Sciences and Engineering Research Council of Canada (NSERC) Post-Graduate Doctoral Scholarship (PGSD2-490318-2016). A.J.T. and G.R.S. acknowledge support from NSERC Discovery Grants (RGPIN-402752-2011 and RGPIN-06569-2016). M.J.M. acknowledges support from a Science and Technology Facilities Council (STFC) Ernest Rutherford Fellowship. D.A. acknowledges support from the Royal Society. G.E.A. is the recipient of an Australian Research Council Discovery Early Career Researcher Award (project number DE180100346) funded by the Australian Government. T.M.B. acknowledges a financial contribution from the agreement ASI-INAF n.2017-14-H.0. P.G.J. acknowledges funding from the European Research Council under ERC Consolidator Grant agreement 647208. S. Markoff and T.D.R. acknowledge support from a Netherlands Organisation for Scientific Research (NWO) Veni Fellowship and Vici Grant, respectively. K.P.M. acknowledges support from the Oxford Centre for Astrophysical Surveys, which is funded through the Hintze Family Charitable Foundation. K.P.M. is currently a Jansky Fellow of the National Radio Astronomy Observatory. This work profited from discussions carried out during a meeting on multi-wavelength rapid variability organized at the International Space Science Institute (ISSI) Beijing by T.M.B. and D. Bhattacharya. The authors acknowledge the worldwide effort in observing this outburst, and the planning tools (created by T. Marsh and coordinated by C. Knigge) that enabled these observations.

Reviewer information *Nature* thanks José L. Gómez and Christopher Reynolds for their contribution to the peer review of this work.

Author contributions J.C.A.M.-J. wrote the manuscript with input from all authors. J.C.A.M.-J. wrote the observing proposal BM421 with help from all authors. G.R.S. wrote the observing proposal BS249 with help from J.C.A.M.-J., A.J.T., R.P.F., P.G.J., G.E.A. and K.P.M. J.C.A.M.-J. designed and processed the VLBA observations. A.J.T. performed the Monte Carlo modelling. J.C.A.M.-J., A.J.T. and G.R.S. analysed the data. M.J.M. led the development of the Lense–Thirring precession scenario, with help from S. Markoff.

Competing interests The authors declare no competing interests.

Additional information
Extended data is available for this paper at https://doi.org/10.1038/s41586-019-1152-0.
Supplementary information is available for this paper at https://doi.org/10.1038/s41586-019-1152-0.
Reprints and permissions information is available at http://www.nature.com/reprints.
Correspondence and requests for materials should be addressed to J.C.A.M.-J.
Publisher's note: Springer Nature remains neutral with regard to jurisdictional claims in published maps and institutional affiliations.

METHODS

V404 Cygni was observed over fifteen epochs with the VLBA, between 17 June and 11 July 2015 (Extended Data Table 1).

Observations and data reduction. External gain calibration was performed using standard procedures within the Astronomical Image Processing System[31] (AIPS). We used geodetic blocks to remove excess tropospheric delay and clock errors for all observations lasting 3 hours or more. Our phase reference calibrator was the bright (1.8 Jy at 15 GHz), nearby (16.6 arcmin from V404 Cygni) extragalactic source J2025+3343 (ref. [32]).

The strong amplitude variability seen in both the VLBA data and the simultaneous data from the Karl G. Jansky Very Large Array (VLA) from 22 June 2015 (ref. [12]) violates a fundamental assumption of aperture synthesis. We therefore broke the data down into short segments, within which the overall amplitude would not change by more than 10%. This equated to 103 scan-based (70-s) segments in the 15-GHz data from 22 June, and two-scan (310-s) segments in the 8.4-GHz data from the other epochs. The sparse coverage in the (u, v) plane in each individual segment meant that we could not reliably image complex structures. We therefore minimized the number of degrees of freedom during deconvolution and self-calibration by performing uv-model fitting using the Difmap[33] software package (v2.41), rather than the standard 'CLEAN' algorithm. With this approach, we found that the source could always be represented by a small number (six or fewer) of point source components. To create the final images, we performed multiple rounds of phase-only self-calibration, and a final single round of amplitude and phase self-calibration (leaving noise-like residuals in all cases).

Given that this version of Difmap did not provide uncertainties on the fitted model parameters, we used the Common Astronomy Software Application[34] (CASA; v4.7.2) to fit the self-calibrated data with the software tool UVMULTIFIT[35]. We used the Difmap model fit results to define both the number of point sources used for each snapshot and the initial guesses for their positions and flux densities.

Given the sparse uv-sampling, we took additional steps to ensure the fidelity of our final images, taking guidance from previous time-resolved VLBI studies[36]. We examined each snapshot image to check for consistency between adjacent frames. Only a small minority of frames showed inconsistent structure, and were therefore reprocessed using prior knowledge from the adjacent frames. In a few cases, we imaged longer chunks of data (10–15 min) to assess the fidelity of the structures with better uv-coverage. As seen in Extended Data Figs. 3–4, the positions and flux densities of our final set of components evolve smoothly with time (other than occasional jumps when a new component appears or a blend of two components separates sufficiently to become resolved). This gives us confidence in the fidelity of our images.

Markov chain Monte Carlo analysis. Short-timescale tropospheric phase variations, particularly at 15.4 GHz, coupled with the propensity of self-calibration to shift source positions by a small fraction of a synthesized beam, combine to introduce low-level positional offsets between individual snapshots. Although these would be averaged out in longer data segments, they affected the fitted component positions in our snapshot images. Furthermore, in snapshots made with fewer than ten antennas (for example, because of the source having set), poor uv-coverage made it hard to distinguish the true source position from the high sidelobes, and the initial peak position selected to start the model-fitting process dictated the astrometric registration of the final image.

To fit for the proper motions of the individual point source components on 22 June, we first had to determine the positional offsets in each snapshot. We assumed ballistic motion and constructed a set of linear equations with k ejecta components and i images, such that:

$$\mathrm{RA}_{ik} = \mu_{\mathrm{RA},k}(t_i - t_{\mathrm{ej},k}) + J_{\mathrm{RA},i} \quad (1)$$

$$\mathrm{Dec.}_{\mathrm{ik}} = \mu_{\mathrm{Dec},k}(t_i - t_{\mathrm{ej},k}) + J_{\mathrm{Dec.},i} \quad (2)$$

where $\mu_{\mathrm{RA},k}$ and $\mu_{\mathrm{Dec.},k}$ represent the proper motions of the kth component, and $t_{\mathrm{ej},k}$ its ejection time. The atmospheric jitter parameters $J_{\mathrm{RA},i}$ and $J_{\mathrm{Dec.},i}$ represent the offsets in position for the ith image, allowing us to correct the positional shifts.

With $k = 10$ moving components (labelled by ejection time and direction of motion; see Extended Data Table 3) and $i = 103$ images, we had 359 individual measurements in both right ascension and declination. This translates to 20 linear equations, and 236 free parameters. We took a Bayesian approach for parameter estimation, simultaneously solving Equations (1) and (2) using a Markov chain Monte Carlo (MCMC) algorithm implemented with the EMCEE package[37]. Prior distributions for all parameters are listed in Extended Data Table 4. Lastly, because of the large number of rapidly moving ejecta and the blending of components close to the core, it was occasionally difficult to distinguish between components. We therefore assigned a confidence flag to each component for each image before the fitting (H, high; M, medium; L, low; B, possible blended component) and weighted the data according to these flags (H = 1, M = 0.7, L = 0.3 and B = 0.1).

The best-fitting results (Extended Data Table 3) were taken as the median of the posterior distributions from the converged MCMC solution, with the 1σ uncertainties reported as the range between the median and the 15th/85th percentile. Two components, N8 and N9, did not appear to move away from the core. This could be due to a recollimation shock in the jet, which is expected to be stationary or even to move upstream briefly[38,39]. However, given the faint nature of the components and the sparse uv-coverage, we caution that this apparent lack of outward movement could instead be an artefact arising from the difficulty of representing complex structures with a small number of unresolved point sources.

Jet dynamics and Doppler boosting. From the similarities in ejection time and position angle, we identified three likely pairs of components (N2/S2, N3/S3 and N6/S6). In all cases, the proper motion of the northern component exceeded that of its southern counterpart, implying that the northern jets are approaching and the southern jets receding. This identification is supported by the first six epochs of our 8.4-GHz VLBA data, which all showed extensions to the north (see Fig. 1), consistent with the northern components being both faster moving and more Doppler boosted. Furthermore, it is only with approaching northern components that we get constraints on $\beta\cos\theta$ for the individual ejecta that are consistent with paired ejections (see Fig. 4). While the component with the highest overall proper motion (S5) is to the south, it could be explained as a relatively fast ($\geq$0.7c) receding ejection at an inclination of 70–80° (Fig. 4). This would be consistent with the variable jet speed and the known precession cone opening angle. The absence of a northern counterpart to S5 could be either because it had not become visible by the end of the observing run, or because of an intrinsic asymmetry in the jets, as suggested for GRO J1655−40 (ref. [40]), and as found in theoretical simulations of warped disks[41].

Assuming that our identification of pairs was correct, we then refit the proper motions of these three pairs, tying the ejection times of each component in a pair. We use the results of these tied fits in Figs. 2–4 and Extended Data Figs. 1–3, and to calculate the jet physical parameters in Extended Data Table 5.

Assuming intrinsically symmetric jets at a distance d, we can determine the jet speed and inclination angle from the proper motions of corresponding approaching and receding components via:

$$\mu^{\mathrm{app}}_{\mathrm{rec}} = \frac{\beta\sin\theta}{1 \mp \beta\cos\theta}\frac{c}{d} \quad (3)$$

$$\beta\cos\theta = \frac{\mu_{\mathrm{app}} - \mu_{\mathrm{rec}}}{\mu_{\mathrm{app}} + \mu_{\mathrm{rec}}} \quad (4)$$

$$\tan\theta = \frac{2d}{c}\frac{\mu_{\mathrm{app}}\mu_{\mathrm{rec}}}{\mu_{\mathrm{app}} - \mu_{\mathrm{rec}}} \quad (5)$$

With a known distance, Equations (4) and (5) can be uniquely solved, allowing us to derive the jet Lorentz factor, $\Gamma = (1 - \beta^2)^{-1/2}$, and the Doppler factors $\delta_{\mathrm{app,rec}} = \Gamma^{-1}(1 \mp \beta\cos\theta)^{-1}$ (see Extended Data Table 5). For unpaired ejecta, we can only solve Equation (3) for $\beta\cos\theta$.

Given our estimated precession cone half-opening angle of roughly 18°, the N2/S2 and N3/S3 pairs have inclinations consistent with being on the surface of a precession cone centred on the binary orbital angular momentum vector, oriented approximately −15° east of north, at an inclination of approximately 50° to the line of sight. However, the N6/S6 pair has a very low inferred inclination of 14.0 ± 0.8°. Either these two ejecta do not form a corresponding pair, or (more likely) the proper motion of N6 is affected by additional, unaccounted systematic uncertainties due to its slow motion and the short lever arm in time (it is based on only six points). Thus, this last pair should be treated as less reliable than the other two. Even should N6 have been ejected slightly later, its observed angular separation suggests an ejection time before 13:40 UT, so our robust upper limit on the precession time scale remains a few hours.

Doppler boosting implies that the ratio of flux densities of corresponding approaching and receding knots, measured at equal angular separation from the core, is given by $S_{\mathrm{app}}/S_{\mathrm{rec}} = (\delta_{\mathrm{app}}/\delta_{\mathrm{rec}})^{3-\alpha}$, where α is the spectral index of the emission. In no case do we measure corresponding knots at the same angular separation, with the southern components all being seen closer to the core than their northern counterparts. Without knowledge of how the intrinsic luminosity of a component evolves with time[42], we cannot use the flux density ratios to independently constrain the Doppler factors of the components.

The nondetection of the northern components close to the core cannot be explained by simple Doppler boosting of intrinsically symmetric jets. Possible alternatives include absorption (intrinsic or external), internal shocks within the jet, external shocks due to interactions with the surrounding medium, increased confinement delaying the time at which the jets became optically thin, or

intrinsic asymmetries in the jets[40,41]. Although breaking the assumption of symmetry could potentially invalidate the kinematic analysis above, the rapidly changing jet orientation remains robust.

Mass-accretion rate. The slim-disk geometry inferred from the X-ray emission implies an accretion rate at or above the Eddington rate. Furthermore, the walls of the slim disk are likely to obscure the hottest inner regions of the accretion flow, implying an intrinsic luminosity higher than the maximum observed value of twice the Eddington luminosity ($2L_{\rm Edd}$)[4]. Furthermore, a supercritical accretion disk is expected to launch a powerful outflow, which can expel a substantial fraction of the infalling mass[19]. Recent X-ray studies of ultraluminous X-ray sources have suggested that the wind kinetic power could be a few tens of times the bolometric luminosity (albeit reduced by the covering factor and solid angle of the wind)[43,44]. The mass accreted during the 2015 outburst was inferred to be a factor of three lower than the mass transferred from the donor star over the preceding 26-year quiescent period[45]. This discrepancy was attributed to substantial wind mass loss, either from the outer disk[29] or from the inner regions[4]. A total outer mass accretion rate of order ten times the Eddington rate would therefore be plausible, and would be sufficient to give rise to a precession period on the order of a minute (Extended Data Fig. 5a).

The average bolometric luminosity over the outburst has been estimated as approximately $0.1L_{\rm Edd}$ (ref. [45]), suggesting that the outer mass accretion rate probably varied substantially. This would alter both the spherization radius and the precession period, and is consistent with the sporadic nature of the marginally detected X-ray QPOs[20]. This could suggest sporadic episodes of precession set by the changing mass-accretion rate through the disk, rather than a long-term, stable, phase-coherent precession. Assuming that the optical polarization (attributed to jet synchrotron emission) reflects the orientation of the jet axis, the slower inferred variation of the optical polarization position angle on 24 June (4° in roughly 30 min)[46] would support this scenario.

Precession mechanisms. Various mechanisms have been put forward to explain X-ray binary jet precession. In the slaved disk model (as applied to SS 433), tidal forces on the equatorial bulge of a misaligned early-type donor cause the star to precess, thereby inducing the disk and jets to precess likewise[47]. However, the predicted precession period[48] for V404 Cygni is about 100 times the 6.5-day orbital period, and cannot explain the observed changes in the jet axis. Alternatively, massive outflows from a radiatively warped, precessing outer disk could collimate and redirect the jets[18]. Existing treatments of radiatively driven warping[49,50] again predict precession periods that are substantially longer than the orbital period, although they were restricted to standard thin accretion disks (with height/radius (H/R) ratios of less than α). For more vertically extended, supercritical disks, the outer disk (where the radiation warping instability acts most strongly) is shielded from the most luminous inner regions by the puffed-up slim disk and the associated clumpy wind outflow, and radiation can be advected with the outflow, making radiative warps unlikely[22].

Resonances between the donor-star orbit and the orbits of disk particles can also cause disk precession, giving rise to superhumps for systems with mass ratios, q, of less than about 0.3 (ref. [51]). However, the predicted periods are a few per cent longer than the orbital period, and again insufficient to explain the rapid changes that we observed. The tidal torque from the secondary is of order 10^{-9} times the Lense–Thirring torque at the spherization radius, so cannot produce the required precession. Finally, given that V404 Cygni is a dynamically confirmed black hole, we can rule out precession driven by magnetic interactions between the compact object and the accretion disk[52].

Predicted precession period. The expected Lense–Thirring precession period (P) for an inner supercritical accretion disk rotating as a solid body is[15,22]:

$$P = \frac{\pi}{3a_*}\frac{GM}{c^3}r_{\rm sph}^3\left[\frac{1-(r_{\rm in}/r_{\rm sph})^3}{ln(r_{\rm sph}/r_{\rm in})}\right]$$

where M is the black-hole mass; a_* is the dimensionless black-hole spin Jc/GM^2 (where J is the spin angular momentum); G is the gravitational constant; and $r_{\rm in}$ and $r_{\rm sph}$ are the inner and outer radii of the slim disk (the latter being the spherization radius), with all radii given in units of the gravitational radius $r_g = GM/c^2$. We assume that $r_{\rm in}$ is located at the innermost stable circular orbit. Given that the structure of the outer part of a supercritical disk is set by the angular momentum carried away by the disk wind, $r_{\rm sph}$ depends on the fraction of the radiation energy ε_w used to launch the wind, as[19]:

$$\frac{r_{\rm sph}/r_{\rm in}}{\dot{m}} \approx 1.34-0.4\varepsilon_w + 0.1\varepsilon_w^2-(1.1-0.7\varepsilon_w)\dot{m}^{-2/3}$$

where $\dot{m}$ is the mass-accretion rate in units of the Eddington rate. The spin parameter of V404 Cygni was estimated[53] as $a_* > 0.92$, but without accounting for the slim-disk geometry (which would require less light bending and hence a lower spin) and assuming the disk inclination to be that of the binary orbit, which our measurements show is not the case. The true spin could therefore be somewhat lower. With a black-hole mass of $12^{+3}_{-2}M_\odot$[8] (where $M_\odot$ is the mass of the Sun), we can estimate the precession time scale of the slim disk for a given wind efficiency, $\varepsilon_w = (1+L_{\rm rad}/L_{\rm wind})^{-1}$, where $L_{\rm rad}$ and $L_{\rm wind}$ are the radiative luminosity and wind power, respectively.

On the basis of the peak intrinsic luminosity[4], and with a wind-power fraction ε_w of 0.25–0.5 (as estimated from relativistic magnetohydrodynamic simulations[54]), slim-disk models imply that $\dot{m}$ is between 15 and 150 (ref. [19]). For moderate spins, we therefore predict precession time scales on the order of minutes and spherization radii of tens to hundreds of r_g (see Extended Data Fig. 5). The predicted spherization radii are consistent with the maximum radius expected for rigid precession[17]. While the 18-mHz QPO detected simultaneously with our observations (at 11:17 UT on 22 June) was of relatively low significance at 3.5σ, it would imply a precession time scale of 56 s. Given the uncertainty in mass-accretion rate and black-hole spin, this time scale is roughly consistent with these predictions. Because the maximum radius for rigid precession implied by the disk alignment criterion sets a spin- and aspect-ratio-dependent lower limit on the precession frequency[17], then for an aspect ratio of height/radius (H/R) = 0.5, this time scale would imply a spin, a_*, of less than about 0.3.

Jet energetics. The minimum amount of energy required to produce a given synchrotron luminosity is[55]:

$$E_{\rm min} \approx 8\times10^6\eta^{4/7}\left(\frac{V}{\rm cm^3}\right)^{3/7}\left(\frac{\nu}{\rm Hz}\right)^{2/7}\left(\frac{L_\nu}{\rm erg\,s^{-1}Hz^{-1}}\right)^{4/7}\rm erg$$

where $\eta = (1+\beta)$ and β is the ratio of energy in protons to that in the radiating electrons, L_ν is the monochromatic radio luminosity (given by $L_\nu = 4\pi\, d^2\, S_\nu$, where S_ν is the measured flux density), ν is the observing frequency and V is the emitting volume. We make the standard assumption that there is no energy in protons ($\eta = 1$). The brightest of our ejecta is knot S3, which at 12:07 UT has a flux density of 461 mJy at 15.26 GHz (Extended Data Fig. 4), and is unresolved to the synthesized beam of 1.2×0.4 mas^2. Assuming a maximum knot radius of 0.4 mas at 2.39 kpc, we derive an upper limit on its minimum energy of 8×10^{38} erg, and a minimum energy field of 2 gauss. This is consistent with the upper limits of 7–400 gauss inferred from assuming that the peak flux density of a component corresponds to the synchrotron self-absorption turnover reaching the observing frequency[42], again assuming a maximum knot radius of 0.4 mas.

Although this knot would have been expanding adiabatically (with an expansion speed of 0.01–0.15c (ref. [12]), it was never resolved to the VLBI beam, so should have been substantially smaller than 0.4 mas at 12:07 UT. Hence the minimum energy is likely to be substantially lower than that derived above. On the other hand, if the magnetic field deviated at all from equipartition, the energy could be somewhat higher than the minimum.

Should the precession period indeed be on the order of minutes, the knots would need to be launched over a time scale small enough that they were not extended substantially by the precessional motion over the launching period. This would argue for ejection on time scales no longer than a few seconds. A lower limit on the time scale comes from the light crossing time of the jet acceleration zone, which was found to be 0.1 light seconds (3×10^9 cm)[56]. Alternatively, modelling the multifrequency radio light curves gave fitted component radii of $0.6–1.3 \times 10^{12}$ cm at the peak of the submillimetre emission in each flare[12], corresponding to light crossing times of 20–40 s. Given that the submillimetre emission does not come from the jet base itself, the time scale of ejection would probably be much shorter. In either case, our minimum energy synchrotron calculations above would not require the jets to exceed the Eddington luminosity. However, even this would not be a hard limit, given recent jet power constraints from ultraluminous X-ray sources[57,58].

Data availability

The raw VLBA data are publicly available from the NRAO archive (https://archive.nrao.edu/archive/advquery.jsp), under project codes BM421 and BS249. All software packages used in our analysis (AIPS, Difmap, CASA, UVMULTIFIT and EMCEE) are publicly available. The final calibrated images and uv-data are available from the corresponding author upon reasonable request. The data underlying the figures are available as csv or xlsx files, and the measured positions and flux densities of all VLBA components from 22 June 2015 are included with the MCMC fitting code (see below).

Code availability

The MCMC fitting code is available at https://github.com/tetarenk/jet-jitter.

31. Greisen, E. W. AIPS, the VLA, and the VLBA. *Information Handling in Astronomy—Historical Vistas*, Vol. 285 (ed. Heck, A.) 109–125 (Astrophysics and Space Science Library, 2003).
32. Ma, C. et al. The international celestial reference frame as realized by very long baseline interferometry. *Astron. J.* **116**, 516–546 (1998).
33. Shepherd, M. C. Difmap: an interactive program for synthesis imaging. *Astronomical Data Analysis Software and Systems VI*, Vol. 125 (eds Hunt, G. & Payne, H.) 77–84 (Astronomical Society of the Pacific Conference Series, 1997).
34. McMullin, J. P., Waters, B., Schiebel, D., Young, W. & Golap, K. CASA Architecture and Applications. *Astronomical Data Analysis Software and Systems XVI*, Vol. 376 (eds Shaw, R. A., Hill, F. & Bell, D. J.) 127–130 (Astronomical Society of the Pacific Conference Series, 2007).
35. Martí-Vidal, I., Vlemmings, W. H. T., Muller, S. & Casey, S. UVMULTIFIT: a versatile tool for fitting astronomical radio interferometric data. *Astron. Astrophys.* **563**, A136 (2014).
36. Fomalont, E. B., Geldzahler, B. J. & Bradshaw, C. F. Scorpius X-1: the evolution and nature of the twin compact radio lobes. *Astrophys. J.* **558**, 283–301 (2001).
37. Foreman-Mackey, D., Hogg, D. W., Lang, D. & Goodman, J. emcee: the MCMC hammer. *Publ. Astron. Soc. Pacif.* **125**, 306–312 (2013).
38. Gómez, J. L., Martí, J. M., Marscher, A. P., Ibáñez, J. M. & Alberdi, A. Hydrodynamical models of superluminal sources. *Astrophys. J.* **482**, L33–L36 (1997).
39. Mimica, P. et al. Spectral evolution of superluminal components in parsec-scale jets. *Astrophys. J.* **696**, 1142–1163 (2009).
40. Hjellming, R. M. & Rupen, M. P. Episodic ejection of relativistic jets by the X-ray transient GRO J1655−40. *Nature* **375**, 464–468 (1995).
41. Fendt, C. & Sheikhnezami, S. Bipolar jets launched from accretion disks. II. The formation of asymmetric jets and counter jets. *Astrophys. J.* **774**, 12 (2013).
42. Miller-Jones, J. C. A., Blundell, K. M. & Duffy, P. Jet evolution, flux ratios, and light-travel time effects. *Astrophys. J.* **603**, L21–L24 (2004).
43. Pinto, C., Middleton, M. J. & Fabian, A. C. Resolved atomic lines reveal outflows in two ultraluminous X-ray sources. *Nature* **533**, 64–67 (2016).
44. Pinto, C. et al. From ultraluminous X-ray sources to ultraluminous supersoft sources: NGC 55 ULX, the missing link. *Mon. Not. R. Astron. Soc.* **468**, 2865–2883 (2017).
45. Ziółkowski, J. & Zdziarski, A. A. Non-conservative mass transfer in stellar evolution and the case of V404 Cyg/GS 2023+338. *Mon. Not. R. Astron. Soc.* **480**, 1580–1586 (2018).
46. Shahbaz, T. et al. Evidence for magnetic field compression in shocks within the jet of V404 Cyg. *Mon. Not. R. Astron. Soc.* **463**, 1822–1830 (2016).
47. Roberts, W. J. A slaved disk model for Hercules X-1. *Astrophys. J.* **187**, 575–584 (1974).
48. Hut, P. & van den Heuvel, E. P. J. Precession and system parameters in early-type binary models for SS 433. *Astron. Astrophys.* **94**, 327–332 (1981).
49. Wijers, R. A. M. J. & Pringle, J. E. Warped accretion discs and the long periods in X-ray binaries. *Mon. Not. R. Astron. Soc.* **308**, 207–220 (1999).
50. Ogilvie, G. I. & Dubus, G. Precessing warped accretion discs in X-ray binaries. *Mon. Not. R. Astron. Soc.* **320**, 485–503 (2001).
51. Whitehurst, R. & King, A. Superhumps, resonances and accretion discs. *Mon. Not. R. Astron. Soc.* **249**, 25–35 (1991).
52. Mushtukov, A. A., Suleimanov, V. F., Tsygankov, S. S. & Ingram, A. Optically thick envelopes around ULXs powered by accreting neutron stars. *Mon. Not. R. Astron. Soc.* **467**, 1202–1208 (2017).
53. Walton, D. J. et al. Living on a flare: relativistic reflection in V404 Cyg observed by NuSTAR during its summer 2015 outburst. *Astrophys. J.* **839**, 110 (2017).
54. Jiang, Y.-F., Stone, J. M. & Davis, S. W. A global three-dimensional radiation magnetohydrodynamic simulation of super-Eddington accretion disks. *Astrophys. J.* **796**, 106 (2014).
55. Fender, R. in *Compact Stellar X-Ray Sources* (eds Lewin, W. & van der Klis, M.) 381–419 (Cambridge Univ. Press, 2006).
56. Gandhi, P. et al. An elevation of 0.1 light-seconds for the optical jet base in an accreting Galactic black hole system. *Nat. Astron.* **1**, 859–864 (2017).
57. Pakull, M. W., Soria, R. & Motch, C. A. 300-parsec-long jet-inflated bubble around a powerful microquasar in the galaxy NGC 7793. *Nature* **466**, 209–212 (2010).
58. Soria, R. et al. Super-Eddington mechanical power of an accreting black hole in M83. *Science* **343**, 1330–1333 (2014).

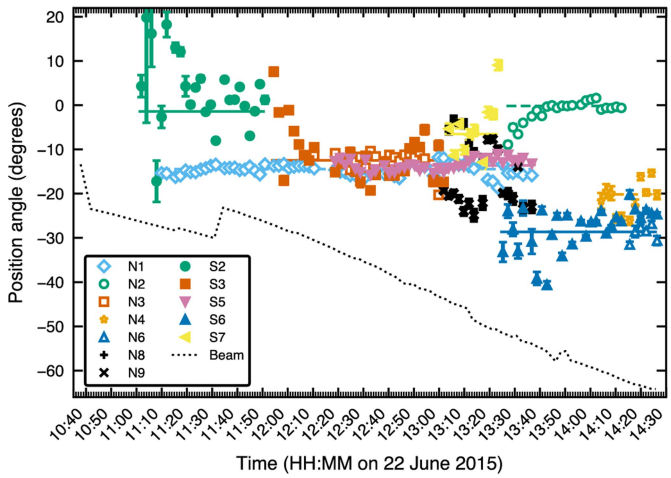

Extended Data Fig. 1 | Position angles of the jet components on 22 June 2015. Angles are shown relative to the jitter-corrected centroid position, with 1σ uncertainties. Corresponding pairs of components (N2/S2, N3/S3 and N6/S6) are shown with matching colours and marker shapes. The mean position angles are shown as dashed (northern components) or solid (southern components) lines. Swings in position angle arise because of components blending as one gives way to another (for example, S2/S3). The dotted black line shows the orientation of the VLBA synthesized beam, which does not match the component position angles. Discrete jumps in beam orientation correspond to antennas entering or leaving the array.

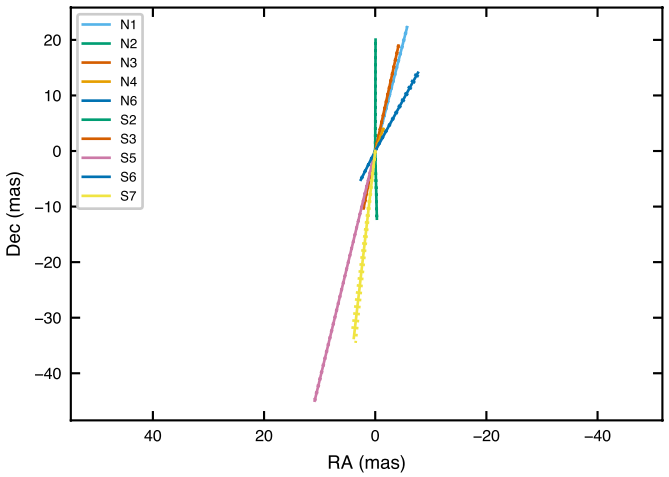

Extended Data Fig. 2 | Best-fitting proper motions of the different components on 22 June 2015. Corresponding pairs of components (N2/S2, N3/S3 and N6/S6) are shown with the same colour. The orientation shows the direction of motion, and the length denotes the magnitude (distance travelled in one day). 1σ uncertainties are indicated by dotted lines (which, given the small uncertainties, merge into the solid lines). The measured position angles range from −0.2° to −28.6° east of north (similar to the range of angles seen over the full outburst duration), providing a lower limit on the precession-cone half-opening angle of 14.2°, consistent with the 18° lower limit inferred from the 8.4-GHz data.

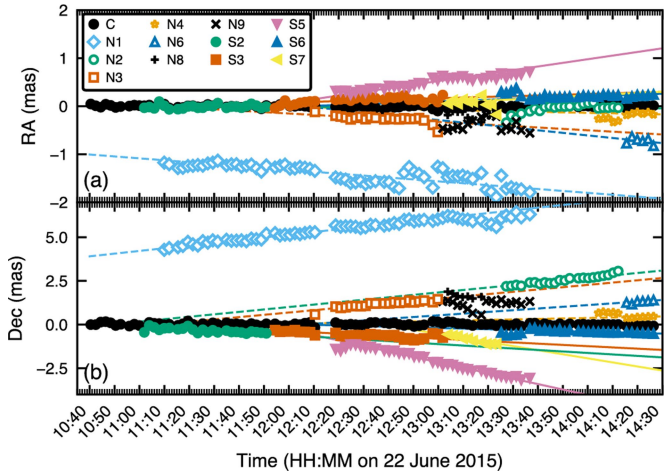

Extended Data Fig. 3 | Motion of the observed components on 22 June 2015. a, **b**, Positions are corrected for atmospheric jitter, and shown in both right ascension (**a**) and declination (**b**), with 1σ uncertainties (often smaller than the marker size). Corresponding pairs of ejecta have matching colours and marker shapes. The core (C) is shown by filled black circles, and does not appear to move systematically over time. The best-fitting proper motions are shown as dashed (northern) and solid (southern) lines. The motion in declination is larger than that in right ascension for all components. Other than N8 and N9, all components move ballistically away from the core.

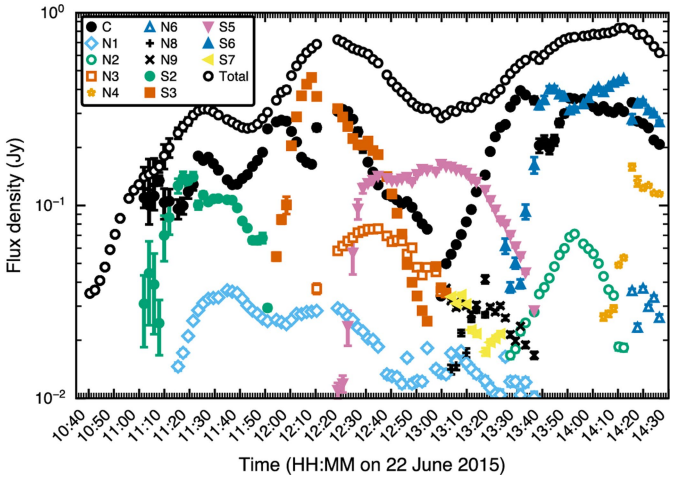

Extended Data Fig. 4 | Light curves for the individual components as a function of time on 22 June 2015. Corresponding pairs of ejecta have matching colours and marker shapes, with empty markers for northern components and filled markers for southern components. Uncertainties are shown at 1σ. The top curve (empty black circles) indicates the integrated 15.4-GHz light curve (including the core source, C).

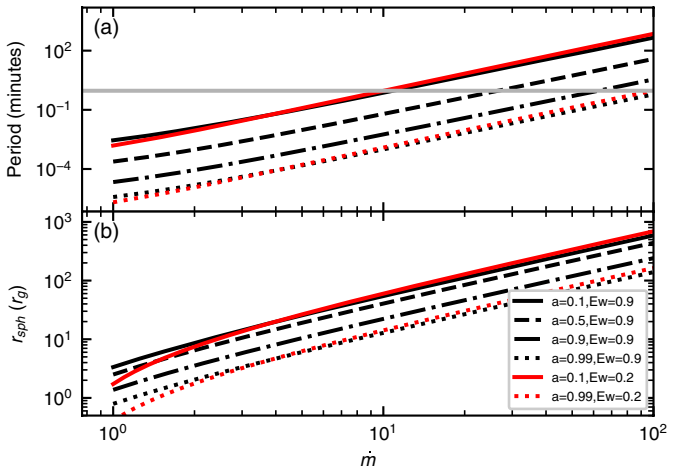

Extended Data Fig. 5 | Slim-disk precession parameters. a, Calculated precession time scales and **b**, spherization radii (where the disk becomes geometrically thicker), as a function of the Eddington-scaled mass-accretion rate, $\dot{m}$, and the dimensionless spin parameter a. Red lines illustrate the minimal impact of changing the fraction ε_w of the accretion power used to launch the inner disk wind. The grey horizontal line in panel **a** shows the 18 mHz frequency of the most compelling X-ray QPO[20]. For precession time scales on the order of minutes, we would need Eddington-scaled accretion rates of 10–100 $\dot{m}_{Edd}$ (depending on the black-hole spin), corresponding to spherization radii of 60–400 r_g.

Extended Data Table 1 | VLBA observing log for the June 2015 outburst of V404 Cygni

Date	Time (UTC)	MJD	Proposal Code	Frequency (GHz)
2015 June 17	09:30–12:30	57190.46±0.06	BM421A	8.4
2015 June 22	10:30–14:30	57195.52±0.08	BS249	15.2
2015 June 23	10:30–13:30	57196.50±0.06	BM421B	8.4
2015 June 24	10:30–13:30	57197.50±0.06	BM421C	8.4
2015 June 26	12:25–14:25	57199.56±0.04	BM421D	8.4
2015 June 27	07:52–09:51	57200.37±0.04	BM421E	8.4
2015 June 30	06:10–08:10	57203.30±0.04	BM421F	8.4
2015 July 1	10:05–12:05	57204.46±0.04	BM421G	8.4
2015 July 2	09:32–11:32	57205.44±0.04	BM421H	8.4
2015 July 4	07:24–09:24	57207.35±0.04	BM421I	8.4
2015 July 5	07:00–09:00	57208.33±0.04	BM421J	8.4
2015 July 6	10:46–12:46	57209.49±0.04	BM421K	8.4
2015 July 7	06:12–10:12	57210.34±0.08	BM421L	22.4
2015 July 8	08:58–10:54	57211.41±0.04	BM421M	8.4
2015 July 11	04:28–07:26	57214.25±0.06	BM421N	4.9

Times denote the on-source time, and do not include the 30-min geodetic blocks at the start and end of the longer observations (those of 3 hours or more). UTC, coordinated universal time.

Extended Data Table 2 | Measured position angles on the plane of the sky for the 8.4-GHz monitoring observations

Date	Position angle
2015 June 17	5.4±0.8
2015 June 23	5.9±1.2
2015 June 24	−0.3±1.1
2015 June 26	1.9±0.9
2015 June 27	−30.6±0.9
2015 June 30	−9.5±0.8

The lower resolution at 8.4 GHz meant that we identified only a single ejection event during each of these epochs, and the proper motions and ejection times could not always be well fit. Position angle is given in degrees east of north.

Extended Data Table 3 | Measured component parameters for the observations of 22 June 2015

Component	Ejection time (UTC hours)	Proper motion (mas day^{-1})	Position angle (degrees E of N)
N1	6.46±0.04	23.02±0.14	−14.45±0.19
N2	10.54±0.03	18.54±0.17	−0.36±0.10
S2	10.36±0.03	7.84±0.21	$-178.56^{+0.31}_{-0.29}$
N3	10.91±0.03	17.09±0.24	−12.31±0.38
S3	11.11±0.02	10.37±0.20	168.36±0.49
N4	11.73±0.03	4.25±0.08	$-20.18^{+1.03}_{-0.98}$
S5	11.847±0.004	46.23±0.17	166.37±0.10
N6	$10.62^{+0.91}_{-0.05}$	9.91±0.16	$-28.61^{+1.14}_{-1.03}$
S6	12.26±0.03	6.28±0.09	153.46±0.77
S7	12.62±0.02	33.86±0.84	$173.47^{+0.73}_{-0.70}$
N2^t	10.799±0.017	20.05±0.12	−0.17±0.06
S2^t	10.799±0.017	12.18±0.29	−178.60±0.15
N3^t	11.128±0.010	19.43±0.12	−12.45±0.18
S3^t	11.128±0.010	10.54±0.10	168.48±0.22
N6^t	12.101±0.032	16.05±0.19	$-28.63^{+0.82}_{-0.79}$
S6^t	12.101±0.032	5.79±0.08	153.39±0.74

N and S denote north- and south-moving ejecta, respectively. From the similarities in their ejection times and position angles, we identify likely pairs of ejecta as N2/S2, N3/S3 and N6/S6. Tying the ejection times of paired components gave the fits in the lower part of the table (denoted by the superscript '*t*'). In cases where the parameters of the independent and tied fits differ substantially, the individual components either had relatively few data (such as N6, with only six points), or little lever arm in angular separation (such as S2, which is only observed close to the core).

Extended Data Table 4 | Prior distributions for the parameters of the atmospheric jitter correction model

Parameter	Description	Prior Distribution	Minimum	Maximum
$\mu_{\rm ra}$	RA proper motion (mas/hr)	truncated normal ($\mu = \mu_{\rm ra,g}$, $\sigma = 0.3$)	-2	2
$\mu_{\rm dec}$	Dec proper motion (mas/hr)	truncated normal ($\mu = \mu_{\rm dec,g}$, $\sigma = 0.3$)	-2	2
$t_{\rm ej}$	Ejection time (decimal hrs)	uniform	t_g-1	t_g+1
$\rm J_{ra}$	RA jitter (mas)	truncated normal ($\mu = \rm J_{ra,core}$, $\sigma = 0.5$)	-3	3
$\rm J_{dec}$	Dec jitter (mas)	truncated normal ($\mu = \rm J_{dec,core}$, $\sigma = 0.5$)	-3	3

Values with a subscript 'g' represent the best initial guess for the parameter values. We use the offset positions (with respect to the centre of the image) of the core jet component to represent the best initial guess for the jitter parameters J_{RA} and J_{Dec}, and to define their priors. All fitted jitter offsets were 2 mas or less.

Extended Data Table 5 | Inferred physical parameters for our identified paired ejecta from 22 June 2015

Ejecta pair	N2/S2	N3/S3	N6/S6
$\mu_{\rm app}$ (mas d^{-1})	20.05±0.12	19.43±0.12	16.05±0.19
$\mu_{\rm rec}$ (mas d^{-1})	12.18±0.29	10.54±0.10	5.79±0.08
$\beta\cos\theta$	0.244±0.011	0.297±0.005	0.470±0.007
β	0.321±0.019	0.351±0.009	0.484±0.007
θ (°)	$40.6^{+2.3}_{-2.5}$	32.5±1.6	14.0±0.8
Γ	1.056±0.005	1.068±0.002	1.143±0.002
$\delta_{\rm app}$	1.253±0.020	1.331±0.010	1.650±0.022
$\delta_{\rm rec}$	0.761±0.008	0.722±0.003	0.595±0.003

$\mu_{\rm app,rec}$ are the approaching and receding proper motions; β is the jet speed as a fraction of the speed of light; θ is the inclination angle of the jet to the line of sight; Γ is the jet bulk Lorentz factor; and $\delta_{\rm app,rec}$ are the approaching and receding jet Doppler factors. In all cases the northern component is believed to be approaching and the southern component receding.